Comparison of Residual Stresses in Inconel 718 Simple Parts Made by Electron Beam Melting and Direct Laser Metal Sintering

L.M. SOCHALSKI-KOLBUS, E.A. PAYZANT, P.A. CORNWELL, T.R. WATKINS, S.S. BABU, R.R. DEHOFF, M. LORENZ, O. OVCHINNIKOVA, and C. DUTY

Residual stress profiles were mapped using neutron diffraction in two simple prism builds of Inconel 718: one fabricated with electron beam melting (EBM) and the other with direct laser metal sintering. Spatially indexed stress-free cubes were obtained by electrical discharge machining (EDM) equivalent prisms of similar shape. The (311) interplanar spacings from the EDM sectioned sample were compared to the interplanar spacings calculated to fulfill stress and moment balance. We have shown that applying stress and moment balance is a necessary supplement to the measurements for the stress-free cubes with respect to accurate stress calculations in additively manufactured components. In addition, our work has shown that residual stresses in electron beam melted parts are much smaller than that of direct laser metal sintered parts most likely due to the powder preheating step in the EBM process.

DOI: 10.1007/s11661-014-2722-2
© The Minerals, Metals & Materials Society and ASM International (outside the USA) 2015

I. INTRODUCTION

POWDER-BASED additive manufacturing has become an increasingly attractive fabrication method in the aerospace and other industries because of the ability to fabricate components heretofore unobtainable with subtractive manufacturing and to reduce the manufacturing time and cost. The ability to fabricate parts from computer-aided design drawings layer by layer opens new avenues to engineering design of components. While process control of the various additive manufacturing methods is evolving (*e.g.*, electron beam melting (EBM) and welding,[1,2] laser metal sintering/melting,[3,4] laser cladding[5]), the main control parameters are typically beam power, speed, material feed rate scanning paths, and preheat temperature. Unfortunately, process control is hindered by indirect parameters within proprietary "black-box" interfaces, which typically require the user to accept limited processing parameter conditions. It is not surprising then that current components have un-optimized microstructures, anisotropic mechanical properties, and significant variations in residual stress.

Residual stress is a common concern amongst the different methods of additive manufacturing of metals. The majority of the resulting residual stresses in metal builds are due to the inherent melt-solidification-state transformation or solid-melt-quench-solid process that occurs on a micro-scale in many components. The semi-serial nature means that even after the first solid-melt-quench-solidification (SMQS), subsequent layers or neighboring regions will reheat and/or partially re-melt prior build areas. The resulting anisotropy is both microstructural (*e.g.*, grain size, defects, precipitates, plastic deformation) and crystallographic (*viz.*, property variation). Further, any thermal expansion mismatch between the base plate material and the build material could create additional residual stress. In part due to the indirect process control interface and plastic strain gradients, residual stress distributions are not the same from material to material and obviously process to

L.M. SOCHALSKI-KOLBUS, is with the Chemical and Engineering Materials Division, Oak Ridge National Laboratory, One Bethel Valley Rd., P.O. Box 2008, MS 6475, Oak Ridge, TN 37830-6475, and also with the Materials Science and Technology Division, Oak Ridge National Laboratory, One Bethel Valley Rd., P.O. Box 2008, Oak Ridge, TN 37830-6430. Contact e-mail: kolbuslm@ornl.gov E.A PAYZANT, Engineering Materials Group Leader, is with the Chemical and Engineering Materials Division, Oak Ridge National Laboratory. P.A. CORNWELL, Scientific Associate, and T.R. WATKINS, Scattering and Thermal Properties Group Leader, are with the Materials Science and Technology Division, Oak Ridge National Laboratory. S.S. BABU, Governorós Chair in Advanced Manufacturing, is with the Manufacturing Demonstration Facility, Oak Ridge National Laboratory, One Bethel Valley Rd., P.O. Box 2008, MS 6479, Oak Ridge, TN 37830-6479, and also with the Department of Aerospace and Biomedical Engineering, University of Tennessee, Knoxville. R.R. DEHOFF, Staff Scientist, and C. DUTY, Senior Staff Scientist, are with the Materials Science and Technology Division, Oak Ridge National Laboratory, and also with the Manufacturing Demonstration Facility, Oak Ridge National Laboratory. M. LORENZ, Scientist, is with the Chemical Sciences Division, Oak Ridge National Laboratory, One Bethel Valley Rd., P.O. Box 2008, MS 6131, Oak Ridge, TN 37830-6131, and also with the National Physics Laboratory, Teddington, U.K. O. OVCHINNIKOVA, Staff Scientist, is with the Chemical Sciences Division, Oak Ridge National Laboratory.

Notice: This manuscript has been authored by UT-Battelle, LLC, under Contract No. DE-AC05-00OR22725 with the U.S. Department of Energy. The United States Government retains and the publisher, by accepting the article for publication, acknowledges that the United States Government retains a non-exclusive, paid-up, irrevocable, world-wide license to publish or reproduce the published form of this manuscript, or allow others to do so, for United States Government purposes.

Manuscript submitted June 11, 2014.
Article published online January 10, 2015

process. Residual stresses have previously been determined in a selected laser melting and selected laser sintering 316L stainless steel sample using X-ray diffraction and the crack compliance method.[6] They showed that the residual stress profile consisted of a thin (~1 mm) layer of tensile stress near the top of the build and near the base plate, while compressive stresses occur in the middle. In addition, the direction of maximum principal stress was shown to be the direction perpendicular to the build direction. In contrast, other studies have determined the residual stresses in SiC150, Stellite 6, and Stellundum 481 that were laser cladded onto a low-carbon steel surface[7] and showed the opposite trend as that of 316L stainless steel fabricated with sintering and melting.[6]

Neutron diffraction provides an ability to non-destructively map residual strains/stresses within the bulk of many materials. Strain, ε, is calculated from a change in length, normalized by the original length. In diffraction, obtaining a representative measure of this "original length" or the strain/stress-free interplanar spacing, d_0, is often not trivial, and the resulting residual stresses are extremely sensitive to this parameter. Methods to determine the reference sample include a far-field measurement where stress is most likely to be negligible, measurement of a powder, measurement of EDM cut cubes or combs for which strain has been mechanically relieved, and calculations based upon force and moment balance.[8,9] Far-field measurements offer a simple solution provided the sample is of the same composition and processing history throughout, but is inappropriate for samples that experience anisotropic heating such as welds. While powders are conceptually appealing because of the inherently stress-free nature of the loose particles, obtaining a metal powder with the same composition, thermal history, microstructure, etc., as the bulk sample is difficult. Powders filed from the parent sample will often exhibit plastic deformation or inter-granular stresses within the particles and annealing such a powder to relieve the stresses can change the phases present or phase fraction relative to the parent sample. A better option is to cut cubes or a comb structure from a similar part, for which the cutting is done carefully as to not introduce any new residual stresses—electrical discharge machining is often used for this purpose. This "spatially-indexed" method[10] is the most accurate and is necessary when there is a chemistry or microstructural gradient in the part of interest, as is the case for welds.[11,12]

For a specimen with randomly oriented grains, a gauge volume of 10^7 crystallites is required in order for a statistically significant amount of crystallites to diffract at an arbitrary sample setting. This number is much greater when texture is present.[13] The selection of a suitable gauge volume that is fully buried for neutron scattering needs to consider these effects—for instance knowing that the EBM process produces larger grains than laser methods,[14] a larger gauge volume will be necessary for the former compared to the latter.

Additively manufactured components typically possess heterogeneous microstructures and possible chemistry variations throughout a build, making the d_0 and residual stress determinations challenging. Although characterization of residual stresses in additive manufactured materials fabricated by different AM methods has been reported,[15–18] a universal quantitative approach to determining a stress-free reference has not yet been established. To date, d_0 assumptions have been made based on a combination of the sample shape, prior process knowledge, and/or the application of force balance. For example, some authors have assumed that one direction of stress was zero based on specific part geometry.[16] Even in such a case, chemistry variations might also have a significant effect on the calculated residual stress.[9,11] Numerically imposing force balance and moment balance through the refinement of d_0 can yield a more accurate stress result. However, it is cautioned that this should not be the only correction employed, as incorrect initial assumptions about the material can potentially generate a false result.[9] For example, a combination of a strain-free reference cube and force balancing to obtain global average d_0 was shown to be the best option for water quenched and aged Ni-based super alloy forging.[19]

In this study, simple shapes of Inconel 718 were fabricated by EBM and direct laser metal sintering (DLMS). The residual stresses were mapped by neutron diffraction. The method of Rolph *et al.* 2013[19] to obtain stresses in forgings was applied to these AM components, employing a force and moment balance method to supplement direct measurements of "spatially-indexed", strain-free (EDM cut) cubes to obtain accurate stress maps.

II. EXPERIMENTAL

A. *Sample Fabrication*

The DLMS samples were provided by Honeywell and the EBM samples were fabricated at the ORNL Manufacturing Demonstration Facility with an Arcam A2. The synthesis parameters are summarized in Table I with the build geometries in Figure 1. The EBM build was fabricated on a 304 stainless steel plate. The composition of the starting powder is within the standard for Inconel 718 with a grain size of 22 to 100 μm. For EBM, the base plate and the precursor powder bed were preheated to 1223 K (950 °C) to decrease thermal gradients during the build. After

Table I. Build Parameters for DLMS and EBM

Method	EBM	DLMS
Average beam speed	5000 mm/s	1200 mm/s
Average melt power	500 W	185 W
Layer thickness	50 μm	20 μm
Hatch spacing*	0.18 mm	0.1 mm
Powder preheat temp.	1223 K (950 °C)	none
Contour thickness	−1 mm	unknown

*The hatch spacing is a measure of the space between the center of the melt pools and their overlap.

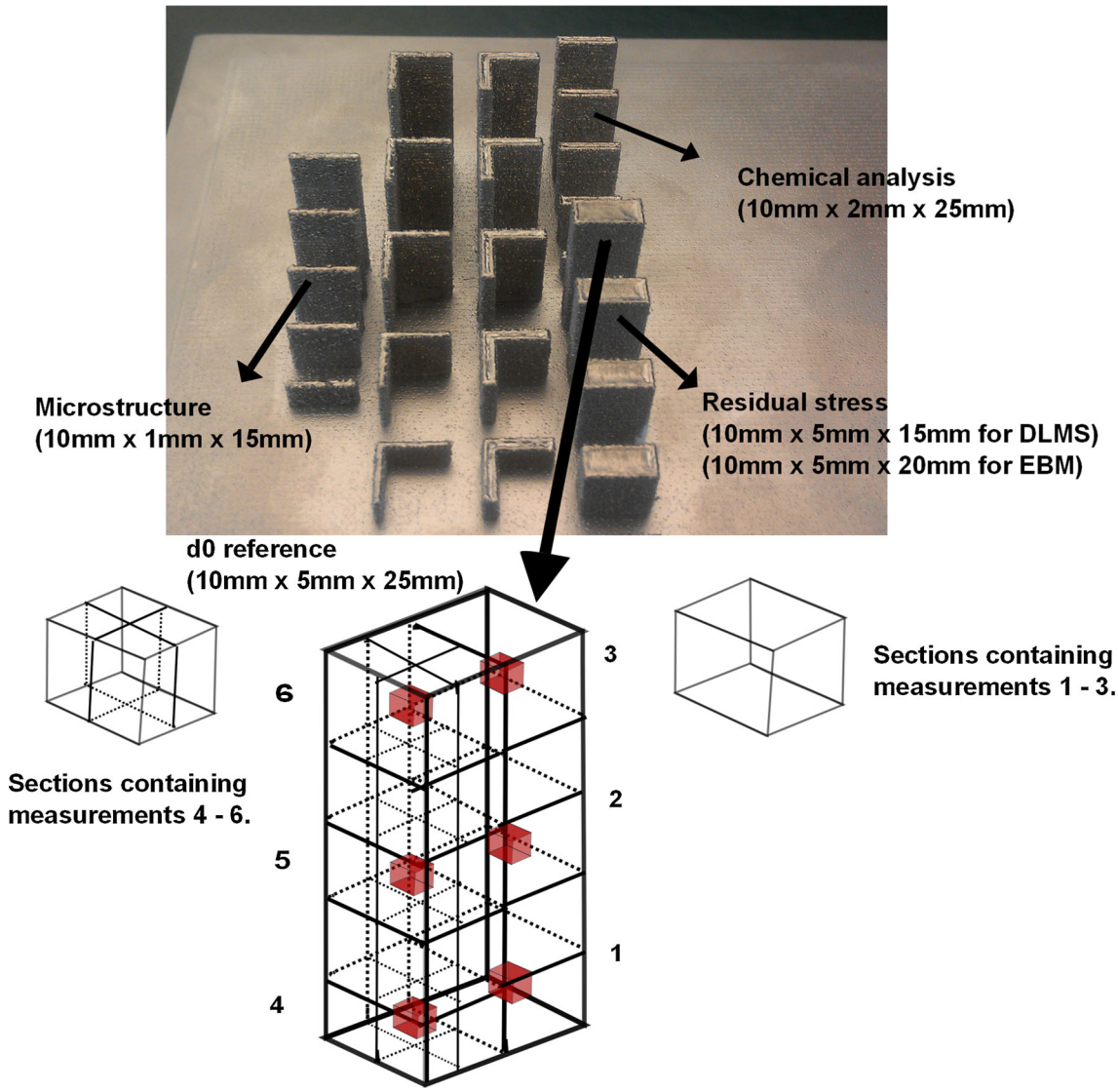

Fig. 1—Samples used for analyses.The top image is the finished build of the electron beam melted parts. The finished DLMS part are similar to this build. The cutting schematic for the d0 references is at the bottom of the figure. The guage volume location for the d0 measurments are shown as red cubes and labelled 1 to 6.

fabrication, all pieces from both builds were removed from the base plate by EDM.

Stress-free references for EBM and DLMS were made from (10 × 5 × 25 mm) prisms which were mechanically relieved of stress by sectioning *via* EDM into ~5 × 5 × 5 mm and ~2.5 × 2.5 × 5 mm prisms, which were reassembled in their original orientation as shown in Figure 1. In both the EBM and DLMS build, we assume that both the unsectioned and sectioned samples have the same microstructure and chemistry gradient (if present) because of their proximity to each other on the build plate and their similar geometries. So, these stress-free references were employed to account for chemistry variations and/or microstructural gradients. A gas atomized precursor powder provided by Pratt and Whitney was measured for comparison—such powders typically have a different microstructure than the finished AM parts.

B. *Residual Strain Measurements*

Neutron diffraction experiments were performed at the neutron residual stress facility 2 (beam line HB-2B) at the high flux isotope reactor (HFIR) at the Oak Ridge National Laboratory. The monochromator was set to a wavelength of ~1.537 Å, placing the (311) reflection at ~ 92 deg 2θ (*i.e.*, near 90 deg to obtain a nearly cubic gauge volume). A gauge volume of 2 × 2 × 2 mm was selected for DLMS, but 3 × 3 × 3 mm was selected for EBM because of the larger grain size to ensure adequate particle statistics. Three *xz*-planes at *y*—1.4, 2.5, and 3.6—were chosen for data collection on the DLMS unsectioned sample with 20 points in each plane. Only one *xz*-plane at $y = 2.5$ was chosen for the EBM sample with 30 points because of the larger gauge volume. These data locations for both the unsectioned DLMS and EBM samples are shown in Figure 2. The quality of

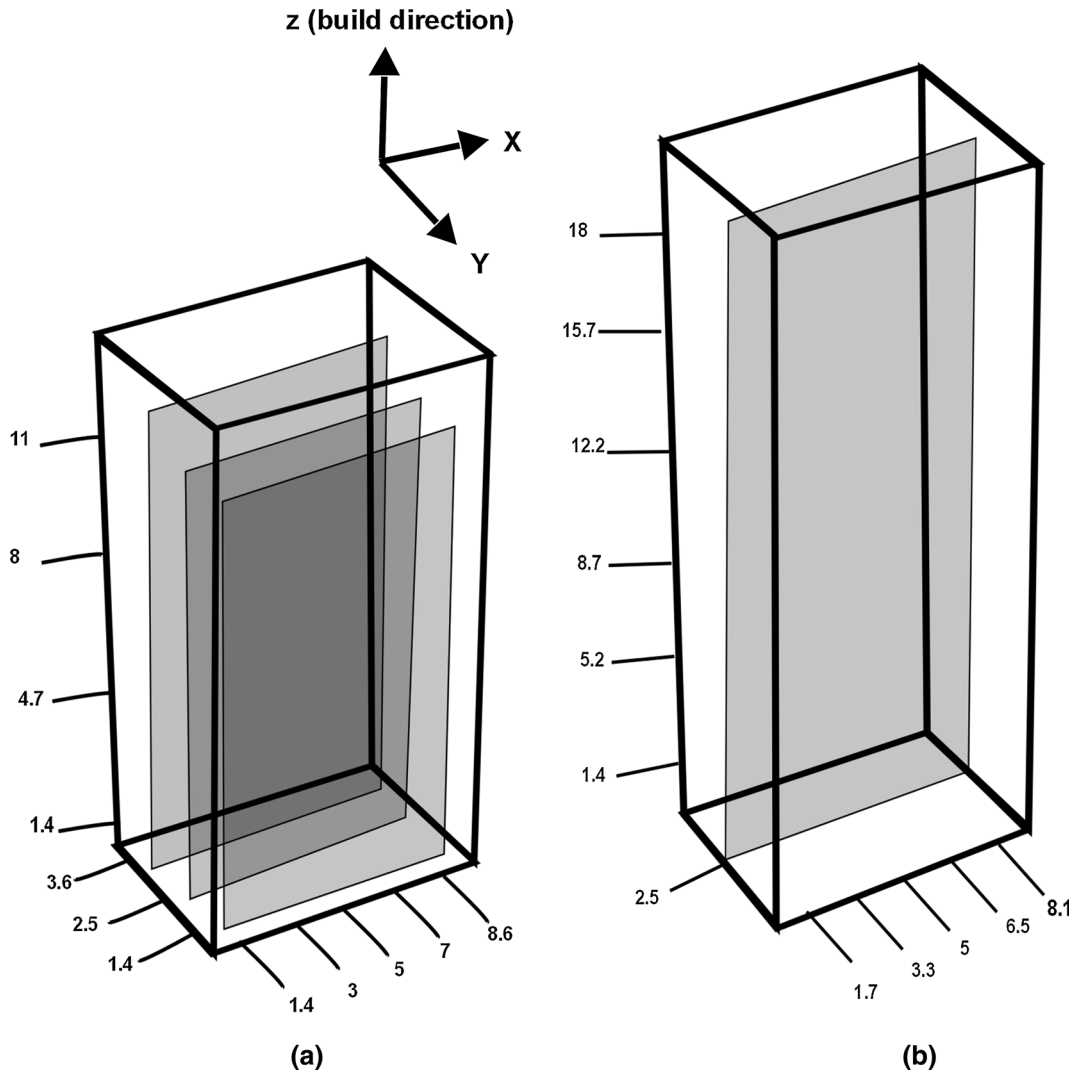

Fig. 2—The 3 XZ-planes chosen for data collection with the respective x, y, and z locations. (*a*) The 5 mm × 10 mm × 15 mm DLMS part. (*b*) The 5 mm × 10 mm × 20 mm EBM part.

the counting statistics was confirmed by observing the intensity of the diffracted peak as the sample was translated through the gauge volume.

The samples were initially aligned optically to a precision of 0.2 mm and selected locations were confirmed using x, y, and z-axis edge scans of the sample though the beam/gauge volume to avoid "pseudo-strains" due to partial gauge volume burial.[20]

C. *Data Analysis*

The strain can be determined with the interplanar spacing, d_{hkl}, as follows:

$$\varepsilon_{hkl} = \frac{d_{hkl} - d_{hkl^0}}{d_{hkl^0}}. \quad [1]$$

Using Hooke's law and the measured strain in three orthogonal directions, the residual stresses, σ_{ii}, in three orthogonal directions (labeled as x, y and z in Figure 1) were calculated as follows:

$$\sigma_{11} = \frac{E}{(1+\nu)(1-2\nu)}[\varepsilon_{11}(1-\nu) + \nu(\varepsilon_{22} + \varepsilon_{33})], \quad [2]$$

$$\sigma_{22} = \frac{E}{(1+\nu)(1-2\nu)}[\varepsilon_{22}(1-\nu) + \nu(\varepsilon_{11} + \varepsilon_{33})], \quad [3]$$

$$\sigma_{33} = \frac{E}{(1+\nu)(1-2\nu)}[\varepsilon_{33}(1-\nu) + \nu(\varepsilon_{11} + \varepsilon_{22})], \quad [4]$$

where E and ν are the Young's modulus and Poisson's ratio (ν) were taken to be 200 MPa and 0.29 deg, respectively. ε_{11}, ε_{22}, and ε_{33} are the orthogonal strain vectors determined using Eq. [1]. Based on the build geometry and knowledge of the thermal history, the principal directions of strain were assumed to be along the x, y, and z axes in Figure 2. The shear strains were not measured and were assumed to be negligible.

As discussed by Hutchings *et al.* 2005,[8] an alternate approach to determine d_0 involves balancing the force

and moment across one or more cross-sections of the sample, as required from mechanical equilibrium. In the present case, an equilibrium approach was used wherein the individual force components are related to the stress by the area perpendicular to the component given by Eq. [5]. In our case, we disregard the area because the area for which the forces are acting upon is a constant (*i.e.*, the gauge volume). Therefore, we will be balancing the residual stresses. The sum of all residual stresses in each orthogonal direction must be equal to zero (Eq. [6]). Similarly, the sum of the moments of inertia in a give plane must be equal to 0 (Eq. [7]).

$$\sigma_{ij} = F_{ij}/\mathrm{A}, \qquad [5]$$

$$\sum \sigma_{11} = 0; \quad \sum \sigma_{22} = 0; \quad \sum \sigma_{33} = 0, \qquad [6]$$

$$\sum \sigma_{11} L_3 = 0; \quad \sum \Sigma\sigma_{22} L_3 = 0; \quad \sum \Sigma\sigma_{33} L_1 = 0, \qquad [7]$$

where $L3$ represents the distance from the origin with z equal to zero in Figure 2 and $L1$ represents the distance from the origin with $x = 0$. All three planes (*XZ, YZ, XY*) were used for moment balance, whereas for only the *XZ*-planes were selected for force balance in both the EBM part and DLMS part because these planes included the most extensive coverage of experimental data. Wolfram Mathematica Version 9 was used to determine the solution for Eq. [5] using a built-in function ("Err (x)") of Wolfram Mathematica v.9 to find the accurate d_0 interplanar spacings for the x, y and z directions.

D. *Microstructure and Chemistry*

A sample from each build with the same geometry (5 mm × 1 mm × 15 mm) was selected for microstructure analysis (10 mm × 1 mm × 15 mm), while the chemical analysis was performed on an EBM specimen only (10 mm × 2 mm × 25 mm). The samples for microstructure were mounted in epoxy, polished and etched with glyceregia. Light optical microscopy was used for imaging at 200×, 500×, and 1000×. The sample chosen for chemical analysis was polished for laser ablation inductively coupled plasma mass spectrometery (LA-ICP MS). Briefly, an Nd:YAG Tempest II laser (New Wave Research, Sunnyvale, CA) operating at 355 nm and 10 Hz was focused onto the sample inside a homebuilt laser ablation cell using a 50-mm focal length quartz lens creating a ~60 μm wide by ~3 μm deep ablation spot. An MS2000 x–y robotic platform (Applied Scientific Instrumentation Inc., Eugene, OR) was used to manipulate the ablation cell with the sample surface at 50 μm/s relative to the stationary laser beam. The ablation cell was continuously purged with 1 L/min argon flow to transport the ablated material directly into the plasma torch of a Thermo iCap Q mass spectrometer (Thermo Scientific, Fremont, CA). All measurements were preformed in kinetic energy discrimination (KED) mode to reduce on molecular interferences.

III. RESULTS

A. *Microstructure*

Figures 3 and 4 are LOM images of the 5 mm × 1 mm × 15 mm geometry for the DLMS build near the top and the bottom of the build plate, respectively. All of the images in Figures 3 and 4 clearly show the individual melt pool solidification structures due to the lack of a preheat treatment to the powder bed before fabrication of each layer. The dark lines between pools are a result of the sintering process where there is less contact between particles as opposed to a melting process. In some areas of the build, there are pores between melt pools. Main FCC γ-phase grains show growth that protrudes through melt pool boundaries and range from 10 to 60 μm in width with respect to build direction and 10 to 100's of microns parallel to the build direction for both the bottom of the build and top of the build. Precipitate phases are seen in Figures 3(b) and 4(b) that occur within the grains and have a small circular or cuboidal morphology. For DLMS, fabricated Inconel 718, γ' ($Ni_3(Al,Ti)$) is the dominate

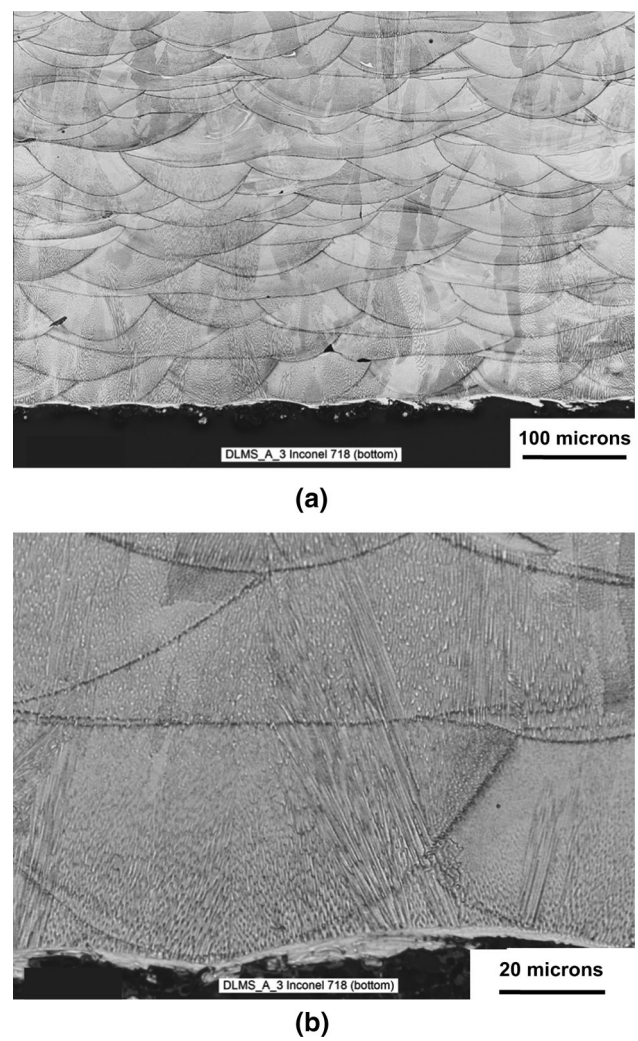

Fig. 3—LOM images of the DLMS sample from the bottom of the build with respect to the build plate. (*a*) 200× (*b*) 1000×.

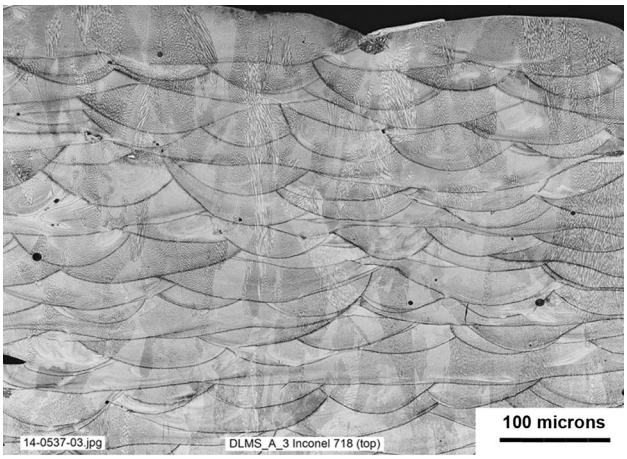

(a)

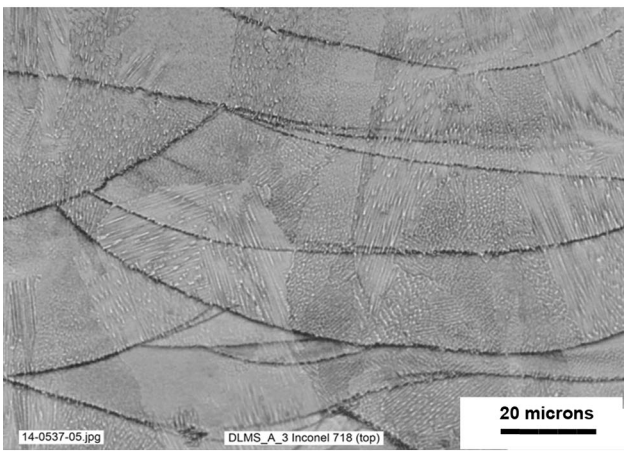

(b)

Fig. 4—LOM images of the DLMS sample from the top of the build with respect to the build plate. (*a*) 200× (*b*) 1000×.

precipitate phase in size and quantity,[4] which is most likely present in the DLMS sample in this study. The overall microstructure between the top and the bottom of the build for the DLMS specimen is essentially the same.

Figures 5 and 6 are LOM images of the 5 mm × 1 mm × 15 mm geometry for the EBM build near the top and bottom of the build plate, respectively. The grain boundaries and solidification structure are not obvious which is an amalgamation of the slow cooling process of EBM and the etchant used. In this case, an electrolytic etchant would be more suitable to see the grain boundaries. In any case, the precipitate phases are obvious, with thin platelet Ni_3Nb δ-phase. γ'' Ni_3Nb phase is present as well, but the grains are typically nanometers in scale for electron beam melted Inconel 718 fabricated with standard parameters,[21] so that phase is not seen in the images. In general, the precipitate morphology is different than that of the DLMS part. Near the bottom of the build, the platelets are relatively small (1 to 2 μm on average) and occur within the γ-phase grains. Near the top of the build, the platelets are much larger and occur along and within the

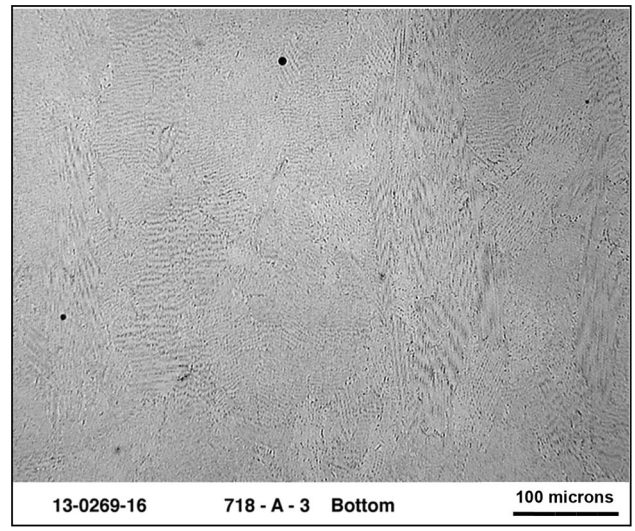

(a)

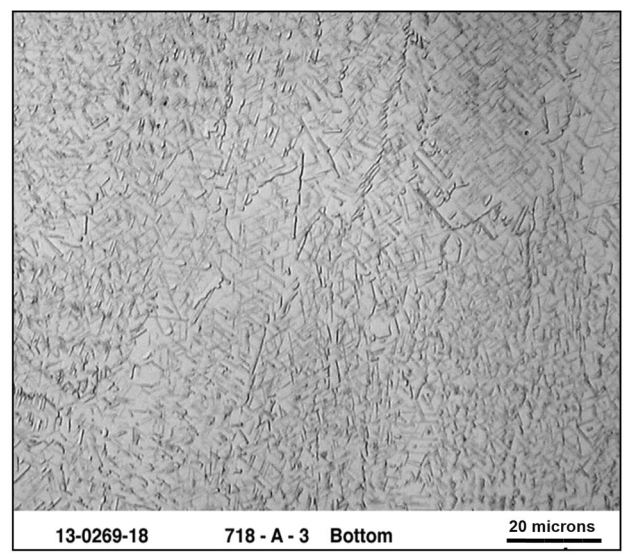

(b)

Fig. 5—LOM images of the EBM sample from the bottom of the build with respect to the build plate. (*a*) 200× (*b*) 1000×.

γ-phase grains. For EBM fabricated Inconel 718, it is common for there to be a microstructural change with respect to the build direction.[22,23] The largest and most numerous precipitate present for the EBM part is the δ-phase[21,23] which we have also shown to be the case in Figures 5 and 6.

B. *Chemistry*

A 60-μm beam width and 3-μm ablation depth was applied to the surface of the 10 mm × 2 mm × 25 mm EBM sample near the top and the bottom of the sample (Figure 7). Five lines of material (each 2 mm long) were ablated in two locations near the top and bottom (Figure 7). Table II shows the selected elements that were analyzed as well as the ratio of the summed intensities between the bottom and the top of the build.

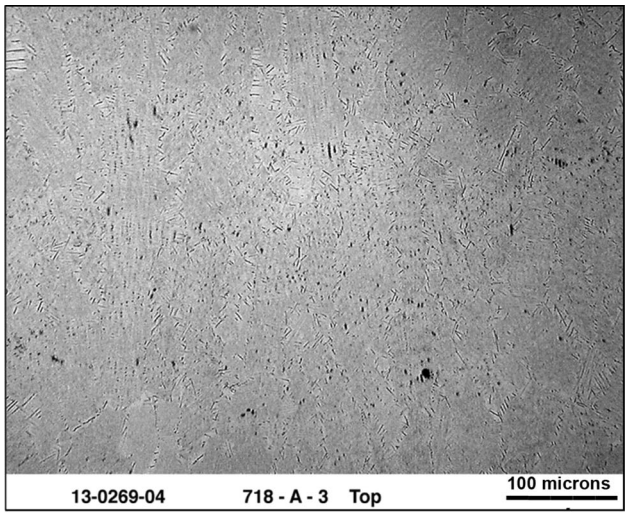

(a)

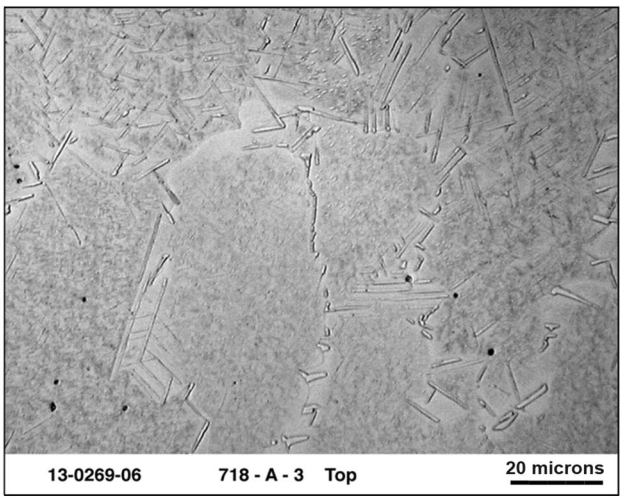

(b)

Fig. 6—LOM images of the EBM sample from the top of the build with respect to the build plate. . (*a*) 200× (*b*) 1000×.

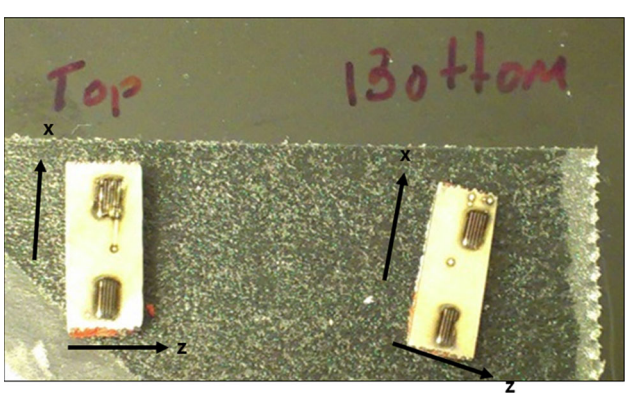

Fig. 7—The EBM sample after LA-ICPMS was performed. The burned areas represent where the ablation occurred.

All elements show a 6 pct or less change from bottom to top with the biggest change seen in Ni (6.3 pct) and Al (3.5 pct). A possible explanation for the increase seen in the Al and Ni content from top to bottom can be explained by the precipitate change from bottom to top of the build in the EBM part (see Figures 5 and 6) with an increase in size of the Ni_3Nb delta phase. It is also possible that there is an increase in the Ni_3Nb y'-phase and Ni3(Al,Ti) y-phase as well, both of which are present in EBM fabricated Inconel 718[21] but detailed analysis has not been performed on the smaller precipitates in these samples. Similarly, Zhang *et al.*[24] have studied laser-cladded IN718 and have shown an increase in elemental segregation into precipitate phases (especially Nb) as a function of heat treatment temperature. Despite the presence of this chemistry change, it is not enough to cause a problem in determining the proper stress-free interplanar spacing.

Table II. The Selected Elements Used in the LA-ICPMS Analysts and the Ratios of Intensity Between the Top and the Bottom of the Build

Element	Ratio Bottom/Top
27AI	0.964990753
48Ti	0.991686178
52Cr	1.029340616
57Fe	1.018447593
60Ni	1.063203954
93Nb	1.019604498
95Mo	1.025040693
181Ta	0.974638035

C. d_0 *Analysis*

The interplanar spacings determined during each sample orientation/strain direction for the DLMS and EBM samples, stressed and stress-free ensemble (d_{0x}, d_{0y} and d_{0z}), are plotted as a function of distance along the build direction, z in Figures 8 and 9. In Figure 8, the interplanar spacings from the stressed prism have a scatter three times that of the stress-free ensemble with the latter located nominally in the middle of the plot. For the stress-free ensemble, the measured d-spacing is independent of the location in the build direction. This suggests that the chemistry gradient is most likely negligible. From the scatter in the stress-free ensemble, we estimated the precision to be ±0.0002 Å. From Figure 9, it is clear that the deviation of the d-spacing of the EBM sample compared to the stress free sample is considerably less than that of the DMLS sample. The points for the stress-free ensemble in Figure 9 show a trend with respect to z-location for each strain direction. Similarly, Rolph *et al.* 2014[19] have shown a similar situation with a change in the d_0 interplanar spacing based on location to a bore in an Inconel 718 forging. Despite the slight change in chemistry from top to bottom of the EBM build, the points in Figure 9 all lie within the error bars, so the trend is not statistically significant.

The results of stress and moment balance for both the EBM part and DLMS part are shown as lines in Figures 8 and 9. In addition to this, the interplanar

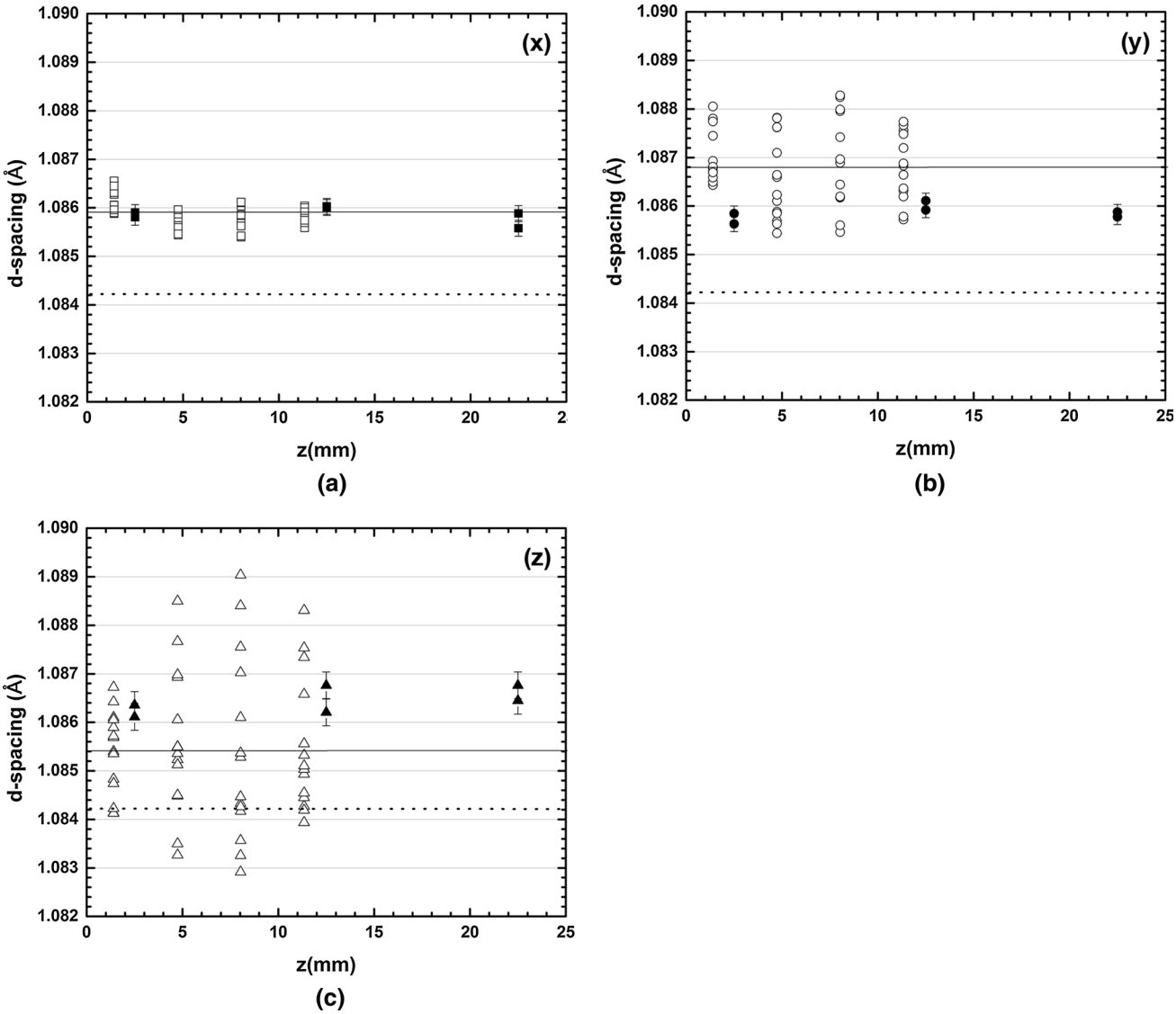

Fig. 8—(311) Interplanar spacing for the 5 mm × 10 mm × 15 mm DLMS unsectioned sample and the reference points (points 1 to 6 from Figure) on the DLMS-sectioned sample. (*a* through *c*) Interplanar spacing for the strain *x*, *y* and *z* directions respectively. Closed symbols represent the reference sample locations (points 1 to 6 from Fig. 2). Open symbols represent the un-sectioned sample. The dotted line is the interplanar spacing measured from the precursor powder and the solid line represents the results from the force and moment balance. Error bars are derived based on the instrumental error.

spacing for the powder was also plotted for comparison. The results for the powder clearly illustrate its unsuitability as a d_0 standard, presumably due to chemistry changes resulting from the AM process. The results for d_{0x} in both Figures 8x and 9x plot well within the data spread for the sectioned blocks. However, d_{0y} and d_{0z} are relatively close to the data but fall a little beyond for the DMLS case: d_{0y} plots at 1 part in 1000 higher interplanar spacings and d_{0z} plots 1 part in 1000 lower which translates into a 100-ppm strain difference for both. There is, therefore, a possibility for microstresses present due to the microstructure, specifically, the grain orientation of the precipitate phases and main FCC γ-phase. It has been shown that intergranular strains can play a large role in the macroscopic stress determined depending on the interplanar spacing measured for several FCC metals.[25,26] Therefore, it is possible that the discrepancy between the experimentally determined d_{0y} and d_{0z} and the force and moment balanced d_{0y} and d_{0z} is due to the plastic deformation anisotropy in the matrix and precipitate phases. This is a common microstress culprit in multi-phase materials.[27]

D. *Residual Stress Analysis*

The stress-free reference value for each strain direction used in Eq. [1] was the average of the *d*-spacings of reference blocks 1 to 6 (see Figure 1). In neutron diffraction, each strain direction gets its own d_0. The measurements performed for each strain direction involved remounting of the sample and d_0 assemblage. This causes a possibility of experimental artifact in one direction versus another. Because of this, it is essential that the d_0 measurements be made during each individual

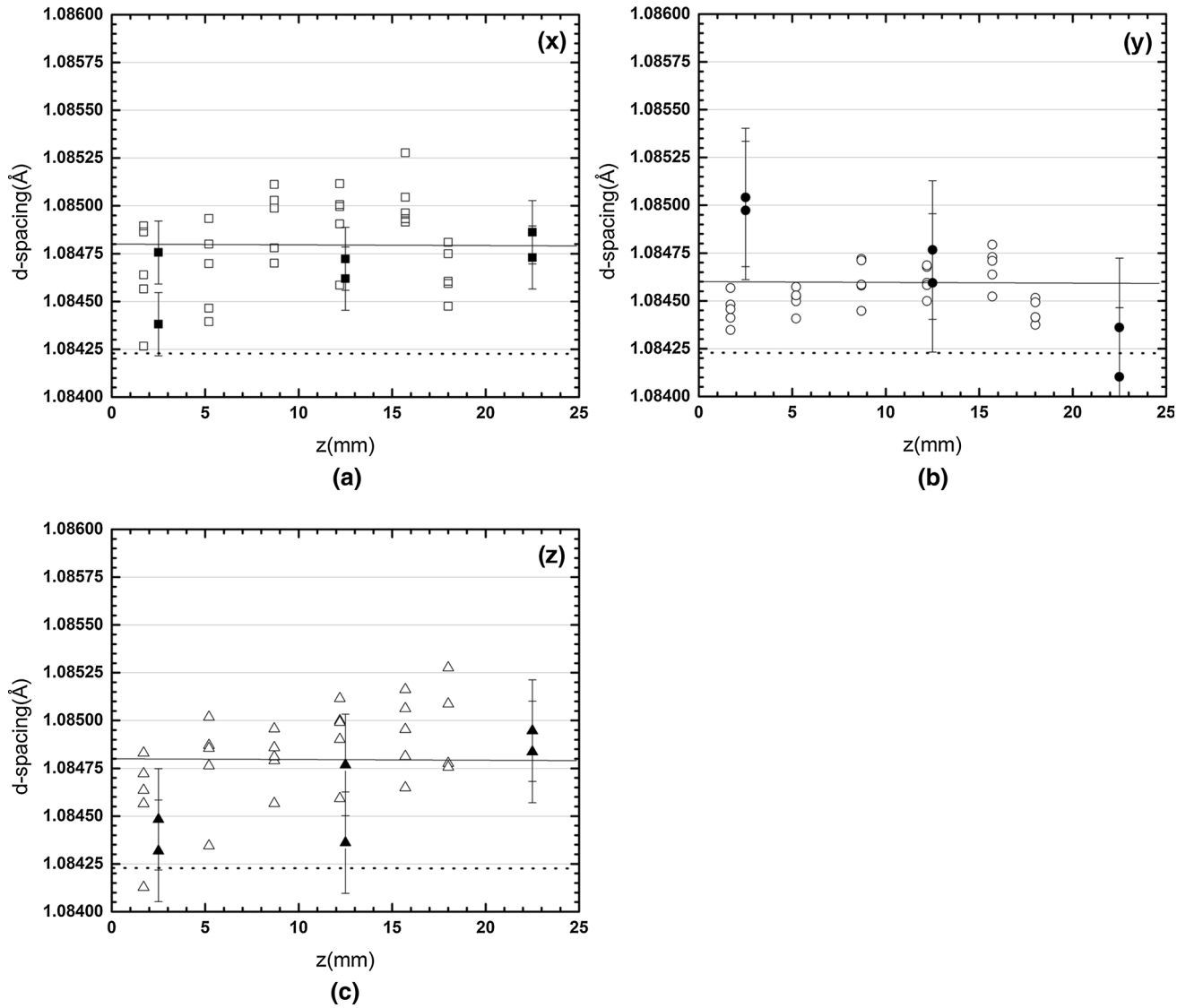

Fig. 9—(311) Interplanar spacing for the 5 mm × 20 mm EBM unsectioned sample and the reference points (points 1 to 6 from Figure) on the EBM-sectioned sample. (*a* through *c*) Interplanar spacing for the strain *x*, *y* and *z* directions respectively. Closed symbols represent the reference sample locations (points 1 to 6 from Fig. 2). Open symbols represent the un-sectioned sample. The dotted line is the interplanar spacing measured from the precursor powder and the solid line represents the results from the force and moment balance. Error bars are derived based on the instrumental error.

strain direction. As such, we had separate reference scans for each sample orientation/strain direction were used (d_{0x}, d_{0y} and d_{0z}) to avoid instrumental errors during the mounting process.

The residual stresses were determined using Eqs. [2] to [4] from these data and shown in Figures 10(a) through (c) and 11(a) through (c). The stress balance method was applied to the interplanar spacings measured in order to refine the d_0 to improve the accuracy of the calculated stresses for each *XZ*-plane (Figure 4), while the moment balance method in Eq. [7] was applied to the *XZ*-, *YZ*- and *XY*-planes. These results are shown in Figures 10(d) through (f) and 11(d) through (f). Figures 10 and 11 show the residual stresses in the *x*-, *y*- and *z* -directions for the center *XZ*-plane for the DLMS part and EBM part, respectively. In general, the residual stresses are much smaller in the EBM part than the DLMS part likely because the DLMS method does not include a preheated base plate or a preheating step before the melt phase in the processing. For the DLMS part, the relative trend of residual stresses shows compressive stress near the center of the build in an ellipsoid distribution. The pattern is not symmetric about the *x*-direction, but it is balanced. These findings (particularly in the stress in the *z*-direction) are similar to residual stresses seen in other materials produced by laser additive manufacturing.[15,17] Recent neutron stress mapping work reported by NIST[17] on DLMS additive-manufactured 17-7 stainless steel is consistent with our results for DLMS Inconel presented in Figure 5, and confirms that the overall nature of the stress distributions in such parts is mainly a function of the manufacturing process for

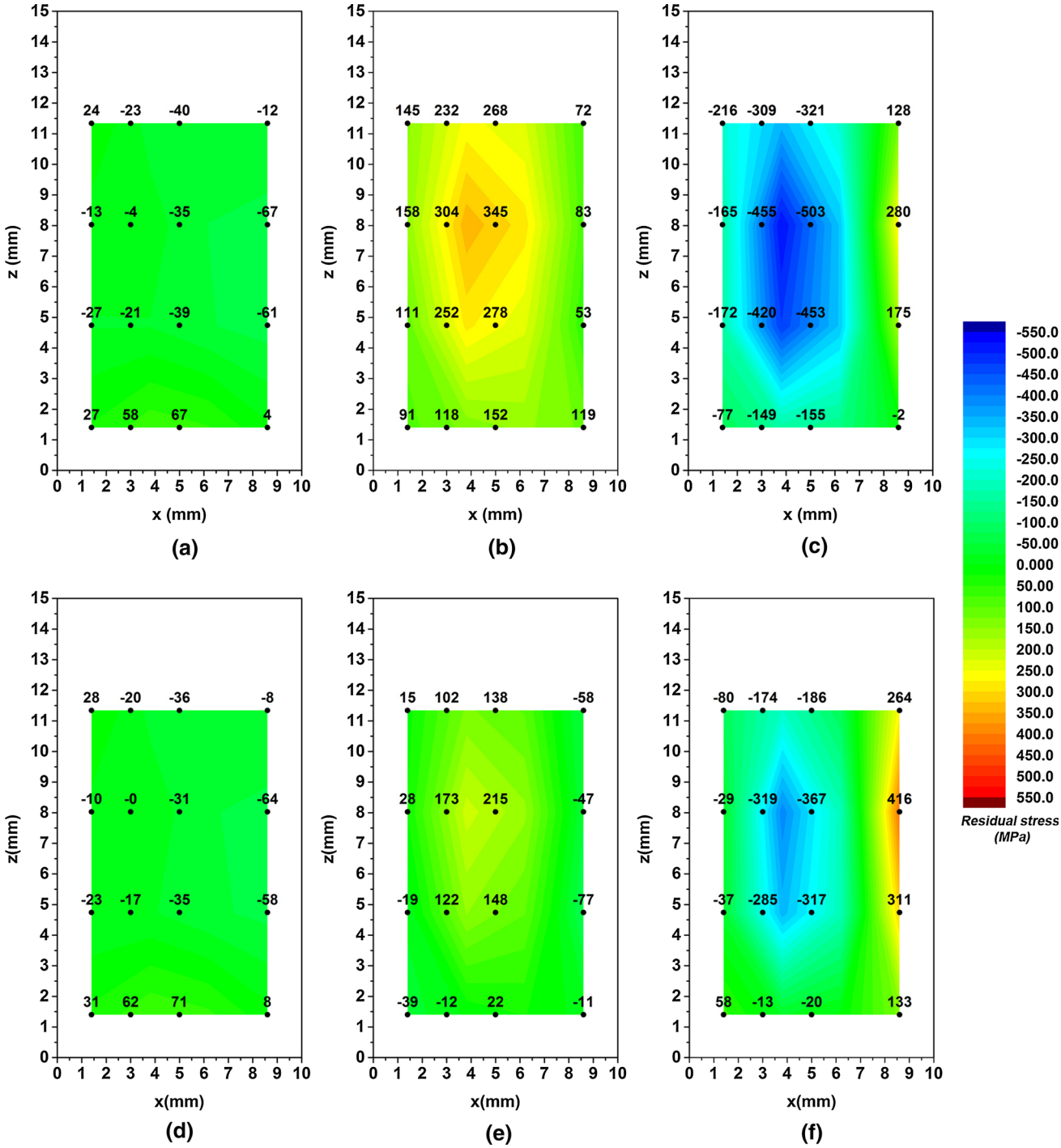

Fig. 10—Residual stress maps for the center *XZ*-plane at $y = 2.5$ mm of the DLMS un-sectioned sample. (*a* through *c*) Residual stress maps for σ_x, σ_y, and σ_z respectively using the average d-spacing of all six reference blocks for each sample orientation/strain direction. (*d* through *f*) Residual stress maps for σ_x, σ_y, and σ_z respectively using the average d_0 values generated after force and moment balance.

austenitic (fcc) iron- and nickel-based alloys. For the EBM part, the residual stress magnitude is smaller and the distribution is different. In general, more tensile stresses are seen in the center of the build and more compressive near the outside. The tensile "spike" near the top right of the build (see stress in *z* in Figure 10) is most likely an artifact due to texture.

IV. DISCUSSION

The microstructure produced from both the DLMS build and EBM build are consistent with what is found in the literature. The coarse columnar grain structure is in part due to the length scale of the cooling process.[23,28] The longer the cooling cycle, the more coarse

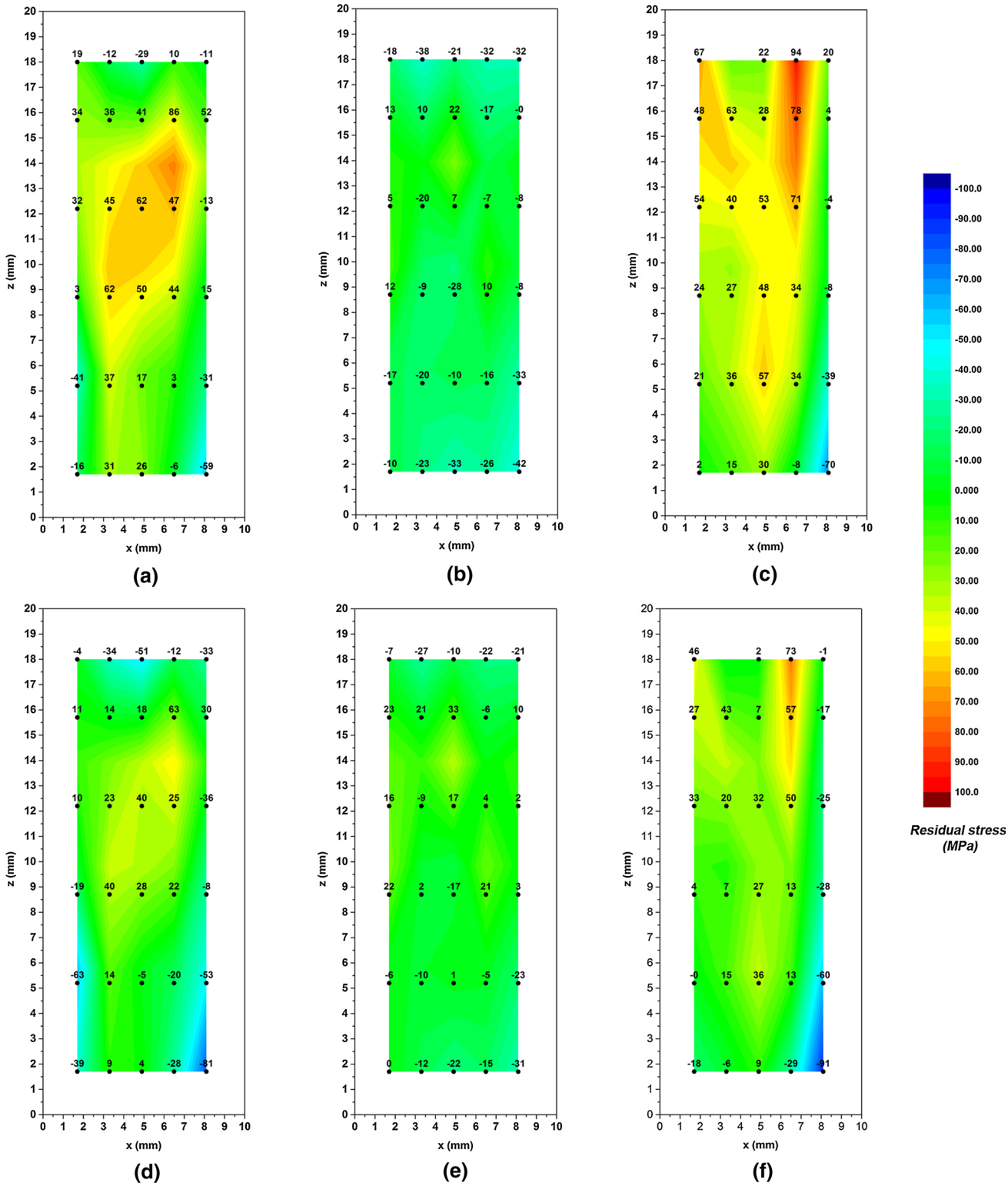

Fig. 11—Residual stress maps of the unsectioned EBM sample. (*a* through *c*) Residual stress maps for σ_x, σ_y, and σ_z respectively using the average d-spacing of all six reference blocks for each sample orientation/strain direction. (*d* through *f*) Residual stress maps for σ_x, σ_y, and σ_z respectively using the average d_0 values generated after force and moment balance.

the columnar grain structure is going to be. While it is known that the DLMS process cools down faster than the EBM process, the modeling tools are not currently capable of simulating these due to the large number of melt runs in both processes. For the EBM build used here, the cooling cycle lasted approximately 8 hours, whereas the cool time for the DLMS build was much shorter which would explain why the columnar grain

structure is coarser for the EBM build. It is difficult to measure the rapid cooling rate of a DLMS build, but based on dendrite arm spacing,[29–31] one can conclude that cooling rates are higher than 100 °C/s which are an order of magnitude higher than EBM. In addition, the EBM build sits encapsulated in heated powder during the cooling cycle and because of this, radiative heat loss dominates and allows for the time for elemental segregation. The substrate temperature in an EBM build previously measured showed slow cooling due to radiation heat transfer in the vacuum chamber.[22] The precipitate that dominates in the EBM build is the δ-phase which is most likely similar to what was reported by Sames *et al*. 2014.

There are several notable aspects of residual stress in the samples studied here. First, we see a change in the residual stress maps when stress and moment balance corrections are applied (Figures 10 and 11). For DLMS, if the stress-free references used in determining the residual stress are not stress and moment balanced, then the stresses in the y-direction are more tensile by 132 MPa on average while the stresses in z are more compressive by 135 MPa on average. The stresses in x are essentially the same which is expected because the average d_{0x} from the measurements is very close to the d_{0x} value determined using the stress and moment balance method. As for the EBM part, the stresses in x are more tensile by 22 MPa on average and the stresses in z are more tensile by 21 MPa on average if the force and moment balance method is not applied. Compared to the DLMS part, the required force and moment balance is considerably smaller. In addition, the chemistry differences in the z-direction are too small to cause any significant difference in the strain measurements, so these offsets are most likely due to the texture of the material. Similar situations have been discussed/reported before, where texture has been related to the predicted response of metals with an applied load.[32,33] In such cases, the presence of crystallographic texture drives the microstructure which then in turn induces microstrains on the system. Of particular interest is the influence of texture in a material on the elastic moduli of the different crystallographic dimensions.[32] Since texture is clearly present in the materials from this study, then it is possible that elastic moduli used in Eqs. [2] through [4] are different than the values used which were most likely determined in materials with no crystallographic texture. Furthermore, the precipitate phases also probably play a role in the residual stress trends because they have a defined orientation with respect to the γ-phase. So, the residual stress left after the thermal cycling the additive processes mostly likely have a different effect in the final part depending on the orientation. This could also cause the discrepancy between balanced and unbalanced residual stresses in the DLMS sample and EBM sample, which are equal but opposite after stress and moment balancing in two different directions (y- and z-). This suggests that the strong crystallographic texture present (002 parallel to the build direction) is a likely candidate for not only the stress difference after the balancing, but also the difference in the d_0 measurements for y and z. Future analysis needs to be done to quantify exactly what effect this specific texture would have in terms of the elastic modulus so that some sort of a correction can be applied to the data. This would include also studying the residual stresses of the precipitate phases as well.

Some other aspects that are also notable are 1. residual stresses are smaller overall for the EBM build, 2. the residual stress changes from the base plate to the top of the build, and 3. the occurrence of tensile stress in the middle of the part for EBM versus compressive stresses for DLMS. Previous studies on DLMS samples that found a similar residual stress pattern in additively manufactured metals attributed this to the behavior of each layer after the melting process has occurred (*e.g.*, thermal shrinkage),[15,16] which is a function of the thermal processes that occur based on what parameters are controlling the melting and cooling cycle. Expanding on previous studies and the results here, the variation in residual stress can be compared to the energy density supplied to a specified melt area. The energy density can vary from method to method (*e.g.*, EBM vs DLMS), because each method requires different input parameters. Therefore, it is reasonable that different residual stress trends occur from method to method. For example, in laser cladding, it was found that providing too much energy density caused delamination of the layers with respect to build direction[34] which is undoubtedly due to high-tensile residual stresses. However, energy density is important in order to build a dense part with minimal porosity. This can be specific challenge for DLMS and EBM, because delamination can also occur if too much energy density is supplied during a build. Both methods contain a set of standards depending on material to optimize the energy density supplied to specific areas of builds for optimal end products. For EBM, this includes a preheat step to the base metal and the powder layer before any melting occurs. This preheat step is meant to decrease the thermal gradient between the base plate and the part being built, which explains why the residual stresses are small for the EBM build (Figure 11). In addition, the DLMS process involves a much quicker cooling step than EBM, so the system is further from equilibrium than in EBM further explaining the larger residual stresses in the DLMS part. Another parameter that is important for build optimization that affects the residual stress is the hatch spacing (which is a measure of the melt pool overlap). Previous studies have shown that more residual stress occurs in the over-lap regions of melt pools because remelting occurs in these areas.[35] Table I shows that the hatch spacing for DLMS build is less than that of EBM build, which helps in explaining why the EBM build shows relatedly more tensile character in the middle parts of the build, while the DLMS shows more compressive stress (Figures 10 and 11).

V. CONCLUSIONS

The residual stresses in EBM parts are much smaller than those in equivalent DLMS parts which is most likely a function of the preheating step, hatching spacing an cooling rate. Both methods contain a set of optimized parameters that aim to produce a pore-free material, but

this is at the possible expense of unwanted residual stress (*i.e.,* DLMS). For both DLMS and EBM, the use of small cubes for which mechanical stresses are relaxed allows for the determination of d_0 with a correction for any chemistry variation indexed to the location of the specimen.[8,10] This method assumes that both the reference material and sample being analyzed for stress contain the same chemistry and microstructure. Both methods have the potential to produce a heterogeneous microstructure and thus a gradient in the stress-free lattice parameter which in turn influences the stress-free reference measurement. On a similar note, the results from this work show that it is important to use small cubes rather than the precursor powder, with multiple measurements. The precursor powder, while assumed unable to sustain macroscopic stress, typically contains significant chemical and microstructural differences from the final parts. This can result in errors 100's of MPa of stress if uncorrected. Further refinement of d_0 for more accurate stress determination can be accomplished using a stress and moment balance method. This method has shown to be a useful tool to identify other possible influences of microstrain on the interplanar spacing. This includes the effect of the crystallographic texture produced from the multiple thermal cycling from both the EBM and DLMS methods here. Further work needs to be conducted to get a better quantitative measure of the effect of crystallographic texture on the macrostrain of additively manufactured metals. Nonetheless, the work has shown that using small indexed cubes is advantageous for the experimenter who can only access certain areas in an additively manufactured part of interest, because it is not required that the entire part be analyzed. The key aspects with respect to stress-free references are to make sure that reference cubes contain a statistically significant number of grains for neutron diffraction, the cube(s) represent the entire area in question, and stress and moment balance is used as a check on the experimentally determined d_0s.

ACKNOWLEDGMENTS

Research at ORNL's High Flux Isotope Reactor was sponsored by the Scientific User Facilities Division, Office of Basic Energy Sciences, and U.S. Department of Energy. Research was also sponsored by the Laboratory Directed Research and Development Program of Oak Ridge National Laboratory, managed by UT-Battelle, LLC, for the U. S. Department of Energy. Research at the Manufacturing Demonstration Facility and High Temperature Materials Laboratory at ORNL was sponsored by the Vehicle Technologies Program, Office of Energy Efficiency and Renewable Energy, U.S. Department of Energy. M. Lorentz and O. Ovichinnikova acknowledge support by the Division of Chemical Sciences, Geosciences, and Biosciences, Office of Basic Energy Sciences, United States Department of Energy under Contract DE-AC05-00OR22725 with Oak Ridge National Laboratory (ORNL), managed and operated by UT-Battelle, LLC. The authors would like to thank Alex Fima at Directed Manufacturing Inc., Fredrick List III and Tom Geer at Oak Ridge National Lab and Andrew Kolbus for their contributions to this work and the samples used.

REFERENCES

1. S.S. Gajapathi, S.K. Mitra, and P.F. Mendez: *Int. J. Heat Mass Transfer*, 2011, vol. 54, pp. 5545–53.
2. S.S. Al-bermani, M.L. Blackmore, W. Zhang, and I. Todd : *Metall. Mater. Trans. A*, 2010, vol. 41A, pp. 3422–34.
3. A. Simchi: *Mater. Sci. Eng. A*, 2006, vol. 428, pp. 148–58.
4. Q. Jia and D. Gu: *J. Alloys Compd.*, 2014, vol. 585, pp. 713–21.
5. S. Safdar, A.J. Pinkerton, L. Li, M.A. Sheikh, and P.J. Withers: *Appl. Math. Model.*, 2012, vol. 37, pp. 1187–95.
6. P. Mercelis and J.P. Kruth: *Rapid Prototyping J.*, 2006, vol. 12, pp. 254–65.
7. J. Grum and M. Žnidaršič: *Mater. Manuf. Process.*, 2004, vol. 19, pp. 243–58.
8. M.T. Hutchings, P.J. Withers, T.M. Holden, and T. Lorentzen: *Introduction to the Characterization of Residual Stress by Neutron Diffraction*, CRC Press, Boca Raton, FL, 2005, pp. 186–197.
9. P.J. Withers, M. Preuss, A. Steuwer, and J.W.L. Pang: *J. Appl. Crystallogr.*, 2007, vol. 40, pp. 891–904.
10. A.D. Krawitz and R.A. Winholtz: *Mater. Sci. Eng. A*, 1994, vol. 185, pp. 123–30.
11. M. Preuss, J.W.L. Pang, P.J. Withers, and G.J. Baxter: *Metall. Mater. Trans. A*, 2002, vol. 33A, pp. 3227–34.
12. N. Iqbal, J. Rolph, R. Moat, D. Hughes, M. Hofmann, J. Kelleher, G. Baxter, P.J. Withers, and M. Preuss: *Metall. Mater. Trans. A*, 2011, vol. 42A, pp. 4056–63.
13. E.H. Kisi and C.J. Howard: *Applications of Neutron Powder Diffraction*, Oxford Univeristy Press, New York, NY, 2008, pp. 420–38.
14. A. Strondl, S. Milenkovic, A. Schneider, U. Klement, and G. Frommeyer: *Adv. Eng. Mater.*, 2012, vol. 14, pp. 427–38.
15. P. Rangaswamy, M.L. Griffith, M.B. Prime, T.M. Holden, R.B. Rogge, J.M. Edwards, and R.J. Sebring: *Mater. Sci. Eng. A*, 2005, vol. 399, pp. 72–83.
16. R.J. Moat, A.J. Pinkerton, L. Li, P.J. Withers, and M. Preuss: *Mater. Sci. Eng. A*, 2011, vol. 528, pp. 2288–98.
17. T. Gnaupel-Herold, J. Slotwinski, and S. Molyan: *AIP Conf. Proc.*, 2014, vol. 1581, pp. 1205–12.
18. T.R. Watkins, H. Bilheux, K. An, A. Payzant, R. Dehoff, C. Duty, W. Peter, C. Blue, and C. Brice: *Adv. Mater. Proces.*, 2013, vol. 171, pp. 23–27.
19. J. Rolph, N. Iqbal, M. Hoffman, A. Evans, M.C. Hardy, M.G. Glavicic, and M. Preuss: *J. Strain Anal. Eng. Des.*, 2014, vol. 48, pp. 221–28.
20. S. Spooner and X. Wang: *J. Appl. Crystallogr.*, 1997, vol. 30, pp. 449–55.
21. K.A. Unocic, L.M. Kolbus, R.R. Dehoff, S.N. Dryepondt, and B.A. Pint: *Corrosion*, 2014, Paper No. 4478.
22. K. Shah, I.U. Haq, A. Khan, S.A. Shah, M. Khan, and A.J. Pinkerton: *Mater. Des.*, 2014, vol. 54, pp. 531–38.
23. W. Sames, K. Unocic, R.R. Dehoff, T. Lolla, and S.S. Babu: *J. Mater. Res.*, 2014, vol. 29, pp. 1920–30.
24. Y Zhang, Z Li, P Nie, and Y Wu: *Metall. Mater. Trans. A*, 2013, vol. 44A, pp. 708–16.
25. J.W.L. Pang, T.M. Holden, and T.E. Mason: *Acta Metall.*, 1998, vol. 46, pp. 1503–18.
26. T.M. Holden, R.A. Holt, and C.N. Tome: *Mater. Sci. Eng. A*, 2000, vol. 282, pp. 131–36.
27. I.C. Noyan and J.B. Cohen: *Residual Stress, Materials Research and Engineering*, Springer , Yorktown Heights, NY, 1987, pp. 52–53.
28. Y. Tan, S. Shi, X. Guo, D. Jiang, W. Dong, and S. Ren: *Vacuum*, 2013, vol. 89, pp. 12–16.
29. A.A. Antonysamy: PhD Thesis, University of Manchester, Manchester, UK, 2012.

30. K. Kempen, E. Yasa, L. Thijs, J.-P. Kruth, and J. Van Humbeeck: *Phys. Proc.*, 2011, vol. 12m pp. 255-263.
31. L. Thijs, F. Verhaeghe, T. Craeghs, J. Van Humbeeck, and J.-P. Kruth: *Acta Mater.*, 2010, vol. 58, pp. 3303–12.
32. M.R. Daymond, C.N. Tome, and M.A.M. Bourke: *Mater. Sci. Forum*, 2000, vols. 347–349, pp. 54–59.
33. J.W. Signorelli, M.A. Bertinetti, and P.A. Turner: *Int. J. Plast.*, 2009, vol. 25, pp. 1–25.
34. Y. Kizaki, H. Azuma, S. Yamazaki, H. Sugimoto, and S. Takagi: *Jpn. J. Appl. Phys.*, 1993, vol. 32, pp. 213–20.
35. F. Liu, X. Lin, G. Yang, M. Song, J. Chen, and W. Huang: *Opt. Laser Technol.*, 2011, vol. 43, pp. 208–13.